APPLICATION OF FRACTAL GEOMETRY METHODS FOR ANALYSIS OF X39Cr13 STEEL AFTER HEAT AND SURFACE TREATMENTS

Monika GWOŹDZIK [1], Mirosław BRAMOWICZ [2], Sławomir KULESZA [3]

[1]*Czestochowa University of Technology, Faculty of Production Engineering and Materials Technology, Institute of Materials Engineering, Czestochowa, Poland, EU*
gwozdzik.monika@wip.pcz.pl

[2]*University of Warmia and Mazury in Olsztyn, Faculty of Technical Sciences, Olsztyn, Poland, EU*
miroslaw.bramowicz@uwm.edu.pl

[3]*University of Warmia and Mazury in Olsztyn, Faculty of Mathematics and Computer Science, Poland, EU*
slawek.kulesza@matman.uwm.edu.pl

Abstract

The paper presents research on fractal analysis of martensitic steel X39Cr13 used for the manufacturing of surgical instruments. Fractal analysis was performed on samples subjected to sequential processes: annealing, surface treatment and sterilization. Annealed samples were tested towards corrosion resistance in physiological solution. Fractal analysis revealed that annealed samples were bifractal, whereas the remaining ones appeared monofractal. Hence, sterilization did not affect the surface morphology of the steel. On the other hand, after corrosion tests there were regular pits several hundreds of micrometers in diameter found in the annealed specimens.

Keywords: X39Cr13 steel, fractal analysis, surface topography

1. INTRODUCTION

Biomedical engineering is the subject of wide interest of many scientific groups (1-6]. Current progress in materials science offers unprecedented perspectives of possible modifications of the materials. Therefore, many attempts have been made to improve mechanical characteristics and corrosion resistance of various materials by using techniques as, for example, nitriding (7]. Martensitic stainless steel has been widely used in industrial processes because of its advantageous properties in this aspect (7-9], similar to austenitic stainless steel that has excellent corrosion resistance (10]. In their recent paper, Luo et al. (10] reported results of comparative study of the sliding wear properties and wear mechanisms of nitrided austenite stainless steel AISI316, with special attention paid to worn surface structural evolution induced by frictional heating and sliding deformation. In turn, Li et al. (7] published results that anodic nitriding treatments were able to produce different types of modified surface layers at different temperatures. The paper (9] presented results of studies on wear resistance of martensitic steel due to modified heat and surface treatment procedures. Most favorable results of wear resistance were obtained for high-temperature tempered and nitrided steel and for high-temperature tempered, nitrided and sterilised steel. At present, the huge development in research equipment has taken place, especially using in surface engineering, such as: SEM, XRD, AFM and TEM (7-21]. The paper presents results of studies of SEM and fractal analysis of martensitic steel after various heat and surface treatment processes.

2. MATERIALS AND EXPERIMENTAL METHODS

Martensitic steel, classified as stainless steel (grade X39Cr13), was selected for testing. The material was delivered in the form of soft annealed sheet (1 mm thick). Specimens were subject to surface treatment in the form of plasma nitriding. The nitriding was carried out at T = 460 ^{o}C and pressure p = 145 Pa for time t = 20 h.

Reactive atmosphere contained 25 % of molecular nitrogen diluted with molecular hydrogen. Part of specimens was sterilized. The sterilization by steam was carried out in an autoclave at T = 134 °C with pressure p = 0.21 MPa for t = 0.5 h for cycles. Apart from that, annealed samples were also tested in Tyrode's physiological solution (pH = 6.8 ÷ 7.4) to determine corrosion resistance. **Table 1** summarizes naming convention of X39Cr13 steel samples.

Table 1 Operating parameters of steel and designation of steel

Sample name	Sample description
A	annealing
A+N	annealing and nitriding
A+N+S	annealing, nitriding and sterilization
A+C(M)	annealing and corrosion test (matrix area)
A+C(P)	annealing and corrosion test (pit area)

Spatial characteristics of the surface texture of steel samples were derived from SEM data using reliable method thoroughly verified in previous studies for SEM as well as AFM images (22, 23]. The routine starts from computation of the autocorrelation map R:

$$\mathrm{R_{mn}} = \frac{1}{2\mathrm{S_q^2}} \sum_{\mathrm{k=1}}^{\mathrm{N-n}} \sum_{\mathrm{l=1}}^{\mathrm{N-m}} \left(\mathrm{z(x+m, y+n) \cdot z(x, y)} \right) \tag{1}$$

where: (m, n) are discrete coordinates of the samples within image, S_q - root-mean-square surface roughness, N - number of scan steps along each direction. Directional inhomogeneities in surface geometry can be expressed in terms of anisotropy ratio S_{tr}, defined as the ratio of extreme correlation lengths S_{a1} and S_{a2}, respectively (24]:

$$\mathrm{S_{tr}} = \frac{\mathrm{S_{a1}}}{\mathrm{S_{a2}}} \tag{2}$$

where: S_{a1}, and S_{a2} - are the shortest and longest decays, respectively. Likewise, half-widths at half maxima (HWHM) of the autocorrelation peak, denoted as w_{a1} and w_{a2}, can be helpful in estimating specific bump size of dominant topographical features d_{av}:

$$d_{av} = w_{a1} + w_{a2} \tag{3}$$

In the next step, 2-dimensional autocorrelation function is averaged around its origin to obtain 1-dimensional autocorrelation profile $R(\tau)$. This profile is directly related to the structure function $S(\tau)$ through the formula (24]:

$$S(\tau) = 2S_q^2 \left(1 - R(\tau)\right) \tag{4}$$

Sayles and coworkers have shown (25] that the structure function reveals specific power-law scaling behavior given by:

$$S(\tau) = K\tau^{2(2-D)} \tag{5}$$

where: D - is the fractal dimension, and K - pseudo-topothesy. Sample plots of profile structure functions are shown in **Figure 1**. In general, D and K correspond to the way, how the relative and absolute height variations maintain scale-invariance, respectively. However, the above allometricity breaks down beyond a certain threshold, referred to as the corner frequency τ_c, at which the plot approaches constant level. On the other

hand, in case of aggregated materials with higher-order alignment patterns, structure function follows two different scaling regimes describing single grains and clusters of grains independently of each other.

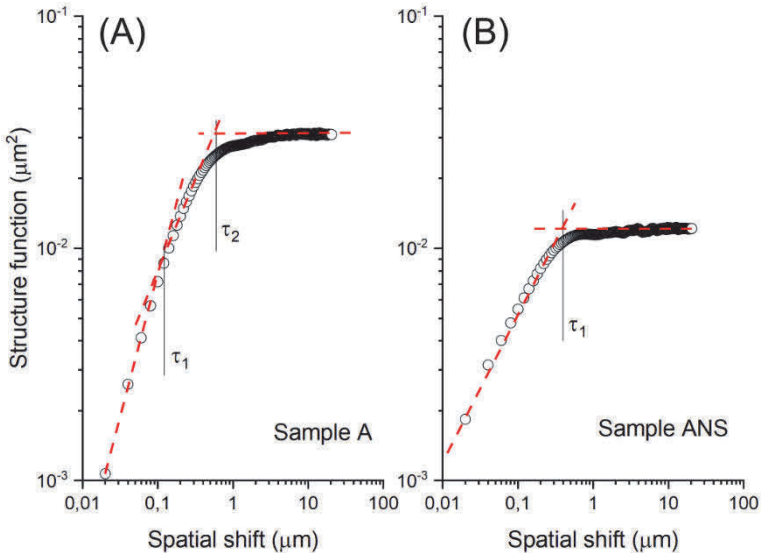

Figure 1 Double-log plots of profile structure functions derived from SEM images of annealed sample exhibiting bifractal behavior (A), and annealed, nitrided and sterilized sample exhibiting monofractal behavior (B)

Apart from fractal parameters, the so-called functional descriptors of topographical complexity can be also derived using the Firestone-Abbott curve (**Figure 2**). Actually, the curve represents cumulative distribution function of relative surface heights plotted in a reverse order. Among others, DIN 4776 standard specifies the three main functional parameters:

- core roughness depth S_k - thickness the flattest part of the bearing curve where the largest increase in surface height exists,
- reduced peak height S_{pk} - thickness of the bearing curve above the core profile,
- reduced valley depth S_{vk} - thickness of the bearing curve below the core profile.

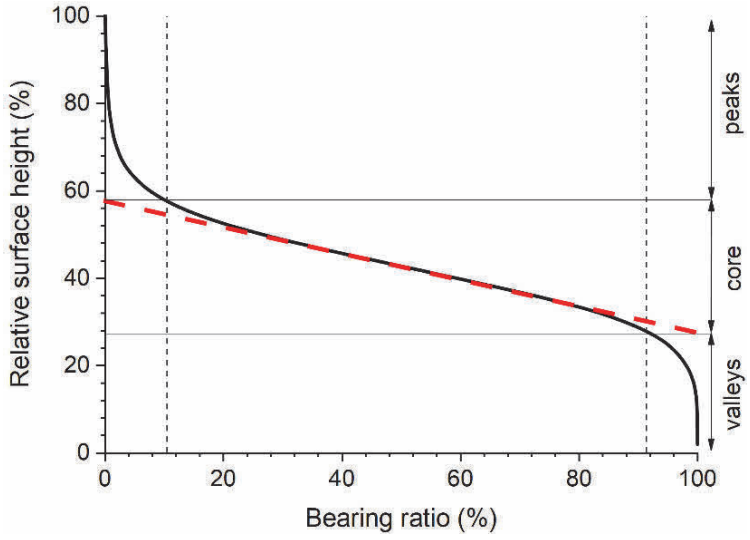

Figure 2 Plot of Firestone-Abbott curve illustrating the concept of estimation of valleys, core and peaks depths measured in SEM images

3. RESULTS OF EXAMINATION

Figure 3 shows SEM images of steel samples subjected to subsequent thermochemical process. **Figure 3A** presents annealed sample with rough surface and small precipitates of the order of hundreds of nanometers wide (sample A). In turn, **Figure 3B** presents the same sample subjected to subsequent nitriding (sample A+N). Diffusion of nitrogen into the surface of steel samples causes significant morphological changes reflected by diminished amplitude of height variations, disappearance of noticeable spatial structures and more homogeneous distribution of small, regular grains. **Figure 3C** shows the sample which was additionally sterilized. Unlike previous process, however, sterilization does not affect the surface morphology of the steel sample. **Figure 4** presents low-magnification SEM image of the annealed sample, which was tested against corrosion. The image reveals the presence of regular pits several hundreds micrometers in diameter and aspect ratio around 2, dug in otherwise flat matrix.

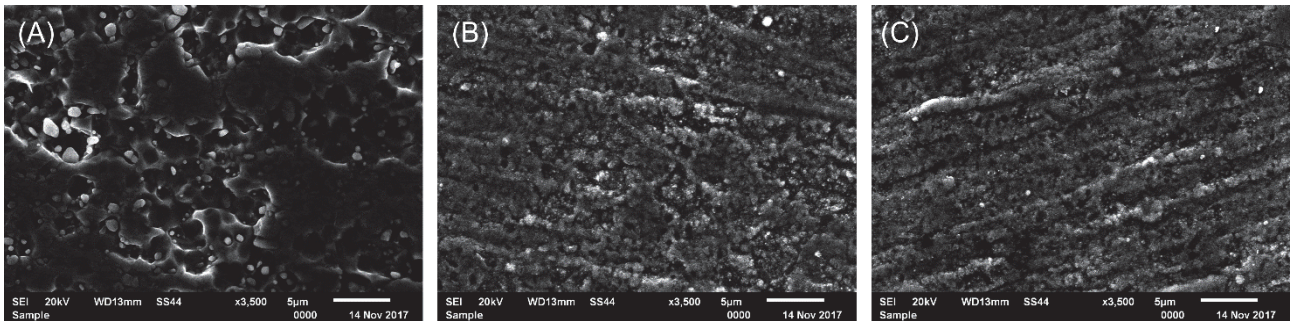

Figure 3 SEM images of the steel samples after various stages of the thermochemical process: (A) annealing, (B) annealing and nitriding, (C) annealing, nitriding and sterilization

Insets in **Figure 4** show detailed structures of solids within both areas exhibiting granular material inside the pit, and almost intact, although grooved surface of the surrounding matrix.

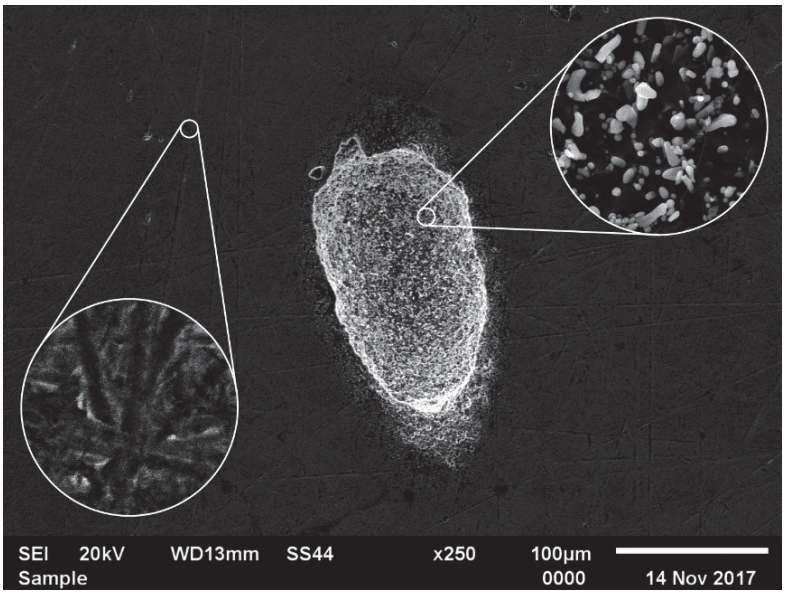

Figure 4 SEM image of the annealed sample subjected to corrosion resistance test exhibiting regular pits etched in otherwise intact steel matrix

Table 2 summarizes various spatial characteristics of the steel samples subjected to subsequent thermochemical treatment, which were derived from SEM images.

Table 2 Spatial characteristics of surface geometry of steel samples at various stages of heat and surface treatments: d_{av} - average bump size, S_{tr} - anisotropy ratio, S_{a1} - the shortest correlation decay length, D - fractal dimension, τ - corner frequency, S_k - core roughness depth, S_{pk} - reduced peak height, S_{vk} - reduced valley depth

Sample	d_{av} (nm)	S_{tr}	S_{a1} (nm)	D_1	τ_1 (nm)	D_2	τ_2 (nm)	S_k (%)	S_{pk} (%)	S_{vk} (%)
A	480	0.75	490	2.41	110	2.59	550	23	76	0.70
A+N	270	0.65	240	2.65	310	-	-	19	73	7.6
A+N+S	270	0.24	250	2.66	300	-	-	20	78	1.8
A+C(M)	270	0.61	270	2.84	110	2.76	520	25	67	8.1
A+C(P)	430	0.91	410	2.30	110	2.55	470	63	37	0.60

Average bump size d_{av} determined from the FWHMs of the autocorrelation function is found to be around 480 nm after annealing, but decreases by a factor of around 2 approaching 270 nm due to nitriding. Subsequent sterilization does not make any further change in this parameter. Note that corrosion test carried out upon annealed sample reveals two different phases concerning bump sizes: matrix appears similar to nitride and sterilized samples, whereas pits resemble annealed sample. Observed trends coincide with changes in anisotropy ratio, which decreases from 0.75 down to 0.24 for annealed (A) and sterilized samples (A+N+S), respectively, but is found nearly identical comparing the same groups of samples. Because determination of the average bump size relies on extreme FWHMs of the autocorrelation function directly associated with the lateral correlation decay lengths, obtained d_{av} values appear nearly equal S_{a1}. When it comes to fractal parameters, annealed sample turns out to be bifractal, whereas nitride and sterilized samples are found monofractal. In case of monofractal samples, fractal dimension D equals to 2.65, and the corner frequency equals to around 300 nm. On the other hand, bifractal sample exhibits less-scalable surface considering both the low- and high-order alignment patterns: 2.41 and 2.59, respectively. Lower corner frequency turns out to be one-third of that in monofractal samples (110 nm), whereas upper corner frequency approaches 550 nm. Nearly identical values for corner frequency can be found in sterilized samples concerning both matrix as well as pit areas. Functional parameters shown in **Table 2** exhibit slightly different trends. The thickness of the core S_k is found to be almost constant through the whole process at around 20 %, as the reduced peak height S_{pk} maintained at around 76 %. In contrast, the reduced valley depth S_{vk} equals around 1 % in annealed and sterilized samples, but increases by a factor of 7 in nitride sample. Observed changes might be due to the fact that reconstruction algorithm turns flat grayscale maps into pseudo-spatial relative heights, hence even small pits in flat surfaces might largely contribute to the cumulative distribution.

4. CONCLUSIONS

The fractal analysis was performed on samples of martensitic steel (X39Cr13) subjected to various thermochemical treatment procedures. The obtained results are as follows:

- Annealed sample exhibits rough surface and small precipitates of the order of hundreds of nanometers in size. Nitriding causes significant morphological changes reflected by diminished amplitude of height variations, disappearance of noticeable spatial structures and more homogeneous distribution of small, regular grains. Sterilization does not affect the surface morphology of the steel. Annealed steel tested against corrosion exhibits regular pits several hundreds micrometers in diameter and aspect ratio around 2, dug in otherwise flat matrix.
- Average bump size d_{av} is found to be around 480 nm after annealing, but decreases by a factor of around 2 approaching 270 nm for surface treatment (A+N and A+N+S). After corrosion, annealed sample reveals two different phases concerning bump sizes: matrix appears similar to samples with

surface treatment, whereas pits resemble annealed sample. An anisotropy ratio S_{tr} is found nearly identical comparing the same groups of samples.

- Annealed sample turns out to be bifractal, whereas nitride (A+N) and sterilized (A+N+S) samples are both monofractal.

REFERENCES

[1] BOSE S., KE D., SAHASRABUDHE H., BANDYOPADHYAY A. Additive manufacturing of biomaterials. *Progress in Materials Science*, 2018, vol. 93, pp. 45-111.

[2] ABDUL HAMID Z. A., THAM C. Y., AHMAD Z., Preparation and optimization of surface-engineered poly(lactic acid) microspheres as a drug delivery device. *Journal of Materials Science. Biomaterials*, 2018, vol. 53, pp. 4745-4758.

[3] SHARMA G., THAKUR B., NAUSHAD M., KUMAR A., STADLER F. J., ALFADUL S. M., MOLA G. T. Applications of nanocomposite hydrogels for biomedical engineering and environmental protection. *Environmental Chemistry Letters*, 2018, vol. 16, pp. 113-146.

[4] TAACA K. L. M., VASQUEZ M. R. Hemocompatibility and cytocompatibility of pristine and plasma-treated silver-zeolite-chitosan composites. *Applied Surface Science,* 2018, vol. 432, pp. 324-331.

[5] KUMAR R., SINGH R., HUI D., FEO L., FRATERNALI F. Graphene as biomedical sensing element: State of art review and potential engineering applications.*Composites Part B: Engineering*, 2018, vol. 134, pp. 193-206.

[6] SKOOG S. A., KUMAR G., NARAYAN R. J., GOERING P. L. Biological responses to immobilized microscale and nanoscale surface topographies. *Pharmacology & Therapeutics,* 2018, vol. 182, pp. 33-55.

[7] LI Y., HE Y., XIU J.J., WANG W., ZHU Y.J. HU B. Wear and corrosion properties of AISI 420 martensitic stainless steel treated by active screen plasma nitriding. *Surface & Coatings Technology*, 2017, vol. 329, pp. 184-192.

[8] GWOŹDZIK M., NITKIEWICZ Z. Topography of X39Cr13 steel surface after heat and surface treatment. *Optica Applicata*, 2009, vol. 39, no. 4, pp. 853-857.

[9] GWOŹDZIK M., NITKIEWICZ Z. Wear resistance of steel designed for surgical instruments after heat and surface treatments. *Archives of Metallurgy and Materials*, 2009, vol. 54, no. 1, pp. 241-246.

[10] LUO Q., OLUWAFEMI O., KITCHEN M., YANG S. Tribological properties and wear mechanisms of DC pulse plasma nitrided austenitic stainless steel in dry reciprocating sliding tests. *Wear*, 2017, vol. 376-377, pp. 1640-1651.

[11] GWOŹDZIK M., KULESZA S., BRAMOWICZ M. Application of the fractal geometry methods for analysis of oxide layer. In *METAL 2017: 26th International Conference on Metallurgy and Materials*. Ostrava: TANGER, 2017, pp. 789-794.

[12] de OLIVEIRA W. R., KURELO B. C. E. S., DITZEL D. G., SERBENA F. C., FOERSTER C. E., de SOUZA G. B. On the S-phase formation and the balanced plasma nitriding of austenitic-ferritic super duplex stainless steel. *Applied Surface Science,* 2018, vol. 434, pp. 1161-1174.

[13] JUNG A., BUCHWALDER A., HEGELMANN E., HENGST P., ZENKER R. Surface engineering of spray-formed aluminium-silicon alloys by plasma nitriding and subsequent electron beam remelting. *Surface & Coatings Technology*, 2018, vol. 335, pp. 166-172.

[14] LU C., YAO J. W., WANG Y. X., ZHU Y. D., GUO J. H., WANG Y., FU H. Y., CHEN Z. B., YAN M. F. A novel anti-frictional multiphase layer produced by plasma nitriding of PVD titanium coated ZL205A aluminum alloy. *Applied Surface Science,* 2018, vol. 431, pp. 32-38.

[15] LIN K., LI X., DONG H., GUO P., GU D. Nitrogen mass transfer and surface layer formation during the active screen plasma nitriding of austenitic stainless steels. *Vacuum*, 2018, vol. 148, pp. 224-229.

[16] SELVABHARATHI R., MURALIKANNAN R. Influence of shot peening and plasma ion nitriding on tensile strength of 2205 duplex stainless steel using A-PAW. *Materials Science & Engineering A*, 2018, vol. 709, pp. 232-240.

[17] ZDRAVECKÁ E., SLOTA J., SOLFRONK P., KOLNEROVA M. Evaluation of the effect of different plasma-nitriding parameters on the properties of low-alloy steel. *Journal of Materials Engineering and Performance*, 2018, vol. 26, pp. 5388-3596.

[18] ESPITIA L. A., DONG H., LI X.Y., PINEDO C.E., TSCHIPTSCHIN A. P. Scratch test of active screen low temperature plasma nitrided AISI 410 martensitic stainless steel. *Wear*, 2017, vol. 376-377, pp. 30-36.

[19] SZAFARSKA M., IWASZKO J. Laser remelting treatment of plasma-sprayed Cr_2O_3 oxide coatings. *Archives of Metallurgy and Materials*, 2012, vol. 57, no. 1, pp. 215-221.

[20] LABISZ K., TAŃSKI T., KREMZER M., JANICKI D. Effect of laser alloying on heat-treated light alloys. *International Journal of Materials Research*, 2017, vol. 108, no. 2, pp. 126-132.

[21] LABISZ K. Microstructure and mechanical properties of high power diode laser (HPDL) treated cast aluminium alloys. *Mat.-wiss. U. Werkstofftech*, 2014, vol. 45, no. 4, pp. 314-324.

[22] KULESZA S., BRAMOWICZ M. Comparative study of correlation methods for determination of fractal parameters in surface characterization. *Applied Surface Science,* 2014, vol. 293, pp.196-201.

[23] NASERI N., SOLAYMANI S., GHADERI A., BRAMOWICZ M., KULESZA S., ŢĂLU Ş., POURREZA M., GHASEMI S. Microstructure, morphology and electrochemical properties of Co nanoflake water oxidation electrocatalyst at micro- and nanoscale. *RSC Advances,* 2017, vol. 7, pp. 12923-12930.

[24] DONG W. P., SULLIVAN P. J., STOUT K. J. Comprehensive study of parameters for characterizing 3-dimensional surface topography IV: Parameters for characterizing spatial and hybrid properties. *Wear*, 1994, vol. 178, no. 1-2, pp. 45-60.

[25] SAYLES R. S., THOMAS T. R. Spatial representation of surface roughness by means of structure function-practical alternative to correlation. *Wear*, 1977, vol. 42, no. 2, pp. 263-276.